

First-order transitions at the Néel temperatures of trigonal SrMn_2P_2 and CaMn_2P_2 single crystals containing corrugated-honeycomb Mn sublattices

N. S. Sangeetha,^{1,*} Santanu Pakhira,¹ Q.-P. Ding,^{1,2} H.-C. Lee,^{1,2}
V. Smetana,³ A.-V. Mudring,³ Y. Furukawa,^{1,2} and D. C. Johnston^{1,2}

¹*Ames Laboratory, Iowa State University, Ames, Iowa 50011, USA*

²*Department of Physics and Astronomy, Iowa State University, Ames, Iowa 50011, USA*

³*Department of Materials and Environmental Chemistry,
Stockholm University, Svante Arrhenius väg 16 C, 106 91 Stockholm, Sweden*

(Dated: May 7, 2021)

Single crystals of CaMn_2P_2 and SrMn_2P_2 were grown using Sn flux and characterized by room-temperature single-crystal x-ray diffraction, electrical resistivity ρ , heat capacity C_p , and magnetic susceptibility $\chi = M/H$ measurements versus temperature T and magnetization M versus applied magnetic field H isotherm measurements. The x-ray diffraction results show that both SrMn_2P_2 and CaMn_2P_2 adopt the trigonal CaAl_2Si_2 -type structure. The $\rho(T)$ measurements demonstrate insulating ground states for both compounds with intrinsic activation energies of 0.124 eV for SrMn_2P_2 and 0.088 eV for CaMn_2P_2 . The $\chi(T)$ and $C_p(T)$ data reveal a weak first-order antiferromagnetic (AFM) transition at the Néel temperature $T_N = 53(1)$ K for SrMn_2P_2 and a strong first-order AFM transition at $T_N = 69.8(3)$ K for CaMn_2P_2 . Both compounds show an isotropic and nearly T -independent $\chi(T \leq T_N)$. ³¹P NMR measurements confirm the strong first-order transition in CaMn_2P_2 but show critical slowing down near T_N for SrMn_2P_2 thus evidencing second-order character. The NMR measurements also indicate that the AFM structure of CaMn_2P_2 is commensurate with the lattice whereas that of SrMn_2P_2 is incommensurate. These first-order AFM transitions are unique among the class of trigonal $(\text{Ca}, \text{Sr}, \text{Ba})\text{Mn}_2(\text{P}, \text{As}, \text{Sb}, \text{Bi})_2$ compounds which otherwise exhibit second-order AFM transitions. This result presents a challenge to understand the systematics of magnetic ordering in this class of materials in which magnetically-frustrated antiferromagnetism is quasi-two-dimensional.

I. INTRODUCTION

The Mn-based 122-type pnictides AMn_2Pn_2 ($A = \text{Ca}, \text{Sr}, \text{Ba}; \text{Pn} = \text{P}, \text{As}, \text{Sb}, \text{Bi}$) have received attention owing to their close structural relationship to high- T_c iron pnictides. The undoped Mn pnictides are local-moment antiferromagnetic (AFM) insulators like the high- T_c cuprate parent compounds [1–3]. The BaMn_2Pn_2 compounds crystallize in the body-centered tetragonal ThCr_2Si_2 structure as in AFe_2As_2 ($A = \text{Ca}, \text{Sr}, \text{Ba}, \text{Eu}$), whereas the $(\text{Ca}, \text{Sr})\text{Mn}_2\text{Pn}_2$ compounds crystallize in the trigonal CaAl_2Si_2 -type structure [4]. Recently, density-functional theory (DFT) calculations for the 122 pnictide family have suggested that the trigonal 122 transition-metal pnictides which have the CaAl_2Si_2 structure might comprise a new family of magnetically-frustrated materials in which to study the potential superconducting mechanism [5, 6]. It had previously been suggested on theoretical grounds that CaMn_2Sb_2 is a fully-frustrated classical magnetic system arising from proximity to a tricritical point [7–9].

The electrical resistivity ρ and heat capacity C_p versus temperature T of single-crystal CaMn_2P_2 were reported in Ref. [10]. The compound is an insulator at $T = 0$ and undergoes a first-order transition of some type at 69.5 K.

Raman spectra of CaMn_2P_2 versus T suggested the formation of a crystallographic superstructure below 69.5 K. However, the authors' magnetic susceptibility $\chi(T)$ measurements revealed no magnetic transition at that temperature. Previous studies on polycrystalline SrMn_2P_2 showed that it is an insulator at room temperature with AFM ordering at $T_N = 53(1)$ K [11]. SrMn_2P_2 transforms from its trigonal CaAl_2Si_2 -type structure at atmospheric pressure p to the tetragonal ThCr_2Si_2 structure (space group $I4/mmm$) after treatment at $p = 5$ GPa and $T = 900^\circ\text{C}$ [12].

Here we report the detailed properties of trigonal Mn pnictides CaMn_2P_2 and SrMn_2P_2 [13] single crystals. We present the results of single-crystal x-ray diffraction, electrical resistivity ρ in the ab plane versus temperature T , isothermal magnetization versus applied magnetic field $M(H)$, magnetic susceptibility $\chi(T)$, heat capacity $C_p(H, T)$, and ³¹P NMR measurements. We find from $C_p(T)$, $\chi(T)$, and NMR that CaMn_2P_2 exhibits a strong first-order AFM transition at $T_N = 69.8(3)$ K whereas SrMn_2P_2 shows a weak first-order transition at $T_N = 53(1)$ K but with critical slowing down on approaching T_N from above as revealed from NMR, a characteristic feature of second-order transitions. Thus the AFM transition in SrMn_2P_2 has characteristics of both first- and second-order transitions. The $\chi(T)$ data also reveal the presence of strong isotropic AFM spin fluctuations in the paramagnetic (PM) state above T_N up to our maximum measurement temperatures of 900 K and 350 K for SrMn_2P_2 and CaMn_2P_2 , respectively, likely

* Present address: Institute for Experimental Physics IV, Ruhr University Bochum, 44801 Bochum, Germany

arising from the quasi-two-dimensional nature of the Mn spin layers [14] together with possible contributions from magnetic frustration.

Remarkably, our studies of SrMn_2P_2 and CaMn_2P_2 reveal the only known members of the isostructural trigonal class of materials with general formula AMn_2Pn_2 containing Mn^{2+} spins $S = 5/2$ that exhibit first-order AFM transitions, where $A = \text{Ca}, \text{Sr},$ or Ba and the pnictogen $Pn = \text{P}, \text{As}, \text{Sb},$ or Bi . The others show second-order AFM transitions, including CaMn_2As_2 [15], SrMn_2As_2 [11, 15, 16], CaMn_2Sb_2 [8, 9, 17–20], SrMn_2Sb_2 [17, 18], and CaMn_2Bi_2 [21]. The AFM transition in the monoclinic compound Li_2MnO_3 containing a Mn honeycomb lattice with Mn^{4+} spins $S = 3/2$ is also second order [22].

Following the experimental details in Sec. II, the single-crystal structure data for single-crystal SrMn_2P_2 and CaMn_2P_2 are given in Sec. III, the $\rho(T)$ data in Sec. IV, our studies of $M(H)$ and $\chi(T)$ in Sec. V, the $C_p(T)$ measurements in Sec. VI, the NMR results in Sec. VII. Concluding remarks are given in Sec. VIII.

II. EXPERIMENTAL DETAILS

Single crystals of SrMn_2P_2 and CaMn_2P_2 were grown in Sn flux. High-purity elements Sr (99.99%) from Sigma Aldrich and Ca (99.98%), Mn (99.95%), P (99.999%), and Sn (99.999%) from Alfa Aesar were taken in the molar ratio (Sr,Ca):Mn:P:Sn = 1.05:2:2:20 and placed in an alumina crucible that was sealed under $\approx 1/4$ atm Ar pressure in a silica tube. Excess Sr or Ca was used in the synthesis to avoid the formation of MnP and thus to enhance the formation of magnetically-pure samples. After preheating the mixture at 600 °C for 7 h, the assembly was heated to 1150 °C at a rate of 50 °C/h and held at this temperature for 15 h for homogenization. Then the furnace was cooled at a rate of 4 °C/h to 700 °C. Shiny platelike hexagon-shaped single crystals of SrMn_2P_2 and CaMn_2P_2 were obtained after decanting the Sn flux using a centrifuge.

Chemical analyses of the single crystals were performed using a JEOL scanning-electron microscope (SEM) equipped with an EDX (energy-dispersive x-ray analysis) detector, where a counting time of 120 s was used. Single-crystal x-ray structural analyses of SrMn_2P_2 and CaMn_2P_2 were performed at room temperature using a Bruker D8 Venture diffractometer equipped with a Photon 100 CMOS detector, a flat graphite monochromator and a Mo K_α $I\mu\text{S}$ microfocus x-ray source ($\lambda = 0.71073 \text{ \AA}$) operating at a voltage of 50 kV and a current of 1 mA. The raw frame data were collected using the Bruker APEX3 software package [23], while the frames were integrated with the Bruker SAINT program [24] using a narrow-frame algorithm integration of the data and were corrected for absorption effects using the multiscan method (SADABS) [25]. The atomic thermal factors were refined anisotropically. Initial models of

the crystal structures were first obtained with the program SHELXT-2014 [26] and refined using the program SHELXL-2014 [27] within the APEX3 software package.

Magnetic susceptibility $\chi = M(T)/H$ at fixed applied magnetic field H over the T range $1.8 \leq T \leq 350$ K and $M(H)$ isotherm measurements for $H \leq 5.5$ T were carried out using a Quantum Design, Inc., Magnetic Properties Measurement System (MPMS). The high-temperature $M(T)$ for $300 \leq T \leq 900$ K was measured using the vibrating sample magnetometer (VSM) option of a Quantum Design, Inc., Physical Properties Measurement System (PPMS). Four-probe dc $\rho(T)$ and $C_p(T)$ measurements were carried out on the PPMS, where electrical contacts to a crystal for the $\rho(T)$ measurements were made using annealed 0.05 mm-diameter Pt wires attached to the crystals with silver epoxy.

The heat-capacity measurements were carried out using the standard semiadiabatic method implemented in the PPMS system by Quantum Design. This technique is widely followed for a second-order magnetic phase transitions and the relative accuracy of the results are within 1%. However, in the present study of thermal hysteresis and latent heat of a first-order magnetic transition, this method does not provide the most accurate results. Therefore, the $C_p(T)$ values associated with the first-order transitions found in CaMn_2P_2 and SrMn_2P_2 were estimated using the single-curve slope analysis method described in Refs. [28–31]. When the sample temperature crosses a first-order transition, the temperature versus time response curve $T(t)$ allows C_p at temperature T to be found from the $T(t)$ data using the relation

$$C_p(T) = \frac{-K_w(T - T_p) + P(T)}{\frac{dT}{dt}(T)}, \quad (1)$$

where, K_w is the thermal conductance of the supporting wires of the sample platform in the heat-capacity puck, T is the temperature of the platform, T_p is the temperature of the heat-capacity puck (system temperature), and P is the heater power. The recent version of MultiVu software is implemented with the single-heat-pulse slope analysis as described in Section 4.6 of Ref. [31]. However, to obtain an accurate value for the latent heat using the slope analysis method, the thermal coupling between the sample and the platform needs to be excellent which can be obtained by applying a very small amount of grease for thermal contact and using a flat thin crystal. The temperature rise of the measurement should be smaller than the width of the peak; otherwise, the heat-capacity peak is artificially broadened. We optimize the temperature rise parameter to obtain the sharpest peak associated with the transition. Figure 1 depicts the measured $C_p(T)$ data around the first order transition for different temperature rise values.

NMR measurements of ^{31}P nuclei with nuclear spin $I = 1/2$ and gyromagnetic ratio $\gamma_N/2\pi = 17.237 \text{ MHz/T}$ were conducted using a lab-built phase-coherent spin-echo pulse spectrometer. Single crystals of SrMn_2P_2 ($4 \times 3 \times 0.1 \text{ mm}^3$) and CaMn_2P_2 ($3 \times 3 \times 0.1 \text{ mm}^3$)

TABLE I. Refined crystallographic parameters obtained from single XRD of SrMn_2P_2 and CaMn_2P_2 crystals. The atomic coordinates in $(\text{Sr}, \text{Ca})\text{Mn}_2\text{P}_2$ of the hexagonal unit cell are Sr/Ca: 1a (0, 0, 0); Mn: 2d (1/3, 2/3, z_{Mn}); and P: 2d (1/3, 2/3, z_{P}).

	SrMn_2P_2	CaMn_2P_2
Structure	CaAl ₂ Si ₂ -type trigonal	CaAl ₂ Si ₂ -type trigonal
Space group	$P\bar{3}m1$	$P\bar{3}m1$
Lattice parameters		
a (Å)	4.656(6)	4.1013(3)
c (Å)	7.138(1)	6.8564(6)
c/a	1.7136(5)	1.6717(3)
V_{cell} (Å ³)	107.27(4)	99.88(2)
Atomic coordinates		
z_{Mn}	0.62033(7)	0.62441(4)
z_{P}	0.2726(1)	0.26155(9)

were used for NMR measurements. ^{31}P NMR spectra were obtained either by fast Fourier transform (FFT) of the NMR echo signals under an external magnetic field of ~ 7.01 T or by sweeping the external magnetic field H at a constant resonance frequency of 121 MHz. The ^{31}P spin-lattice relaxation rate ($1/T_1$) was measured with a saturation recovery method. $1/T_1$ at each T was determined by fitting the nuclear magnetization M versus time t using the stretched exponential function $1 - M(t)/M(\infty) = e^{-(t/T_1)^\beta}$, where $M(t)$ and $M(\infty)$ are the nuclear magnetization at time t after the saturation and the equilibrium nuclear magnetization at $t \rightarrow \infty$, respectively. All the relaxation data were well fitted with the stretched exponent $\beta = 1$ in the paramagnetic state for both samples. In the AFM state, $\beta \sim 0.6 \pm 0.15$ was used for SrMn_2P_2 . For CaMn_2P_2 in the AFM state, $\beta = 1$ was used. However, at low temperatures below ~ 20 K, we observed a slight deviation from the function and fitted with two T_1 components and took the long component as T_1 .

III. CRYSTAL STRUCTURE

SEM images of the crystal surfaces indicated single-phase crystals. EDX analyses of the chemical compositions were in agreement with the expected 1:2:2 stoichiometry of the compounds and the amount of Sn incorporated into the crystal structure from the Sn flux is zero to within the experimental error.

Single-crystal XRD measurements on CaMn_2P_2 and SrMn_2P_2 confirmed the single-phase nature of the compounds and the CaAl₂Si₂-type crystal structure of each that is shown in Fig. 2. The crystal data are listed in Table I. The lattice parameters a and c of the trigonal struc-

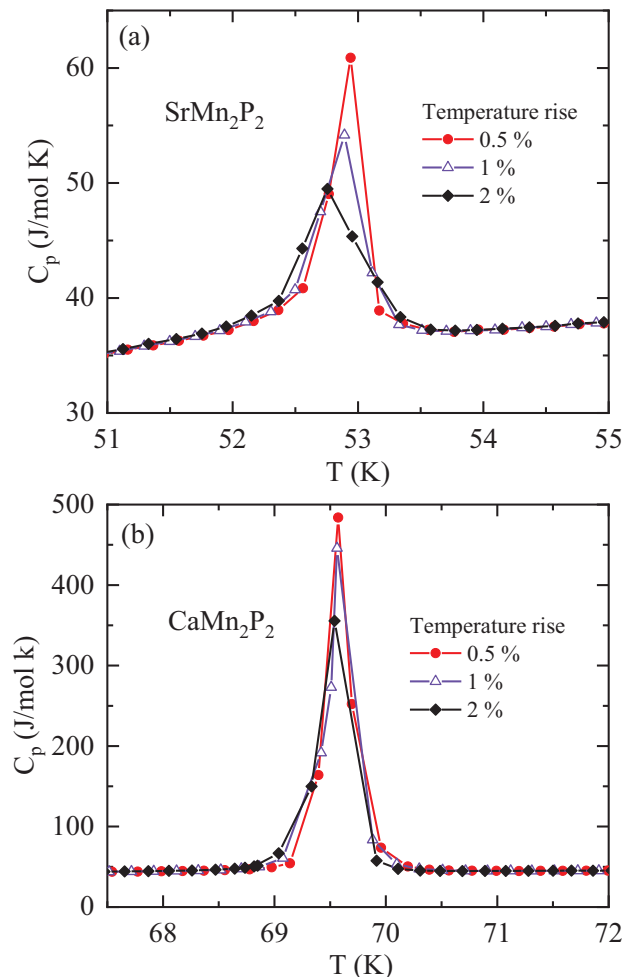


FIG. 1. Measured $C_p(T)$ data of (a) SrMn_2P_2 and (b) CaMn_2P_2 single crystals around FOMT for different temperature-rise values using standard semi-adiabatic method implemented in the PPMS system by Quantum Design.

ture (hexagonal unit cell) are in good agreement with previous values [10, 13]. The crystal structure of CaMn_2P_2 at 293 and 40 K was found to be the same [10]. However, as noted in the Introduction, Raman spectra of CaMn_2P_2 versus T suggested the formation of a crystallographic superstructure below 69.5 K, which was stated to be consistent with the authors' single-crystal x-ray diffraction data [10].

IV. ELECTRICAL RESISTIVITY

The ab -plane $\rho(T)$ data from 270 to 400 K for SrMn_2P_2 and from 150 to 300 K for CaMn_2P_2 are shown in Figs. 3(a) and 3(b), respectively. For both compounds ρ first increases slowly with decreasing T and then increases more rapidly. The data demonstrate that both SrMn_2P_2 and CaMn_2P_2 have insulating ground states.

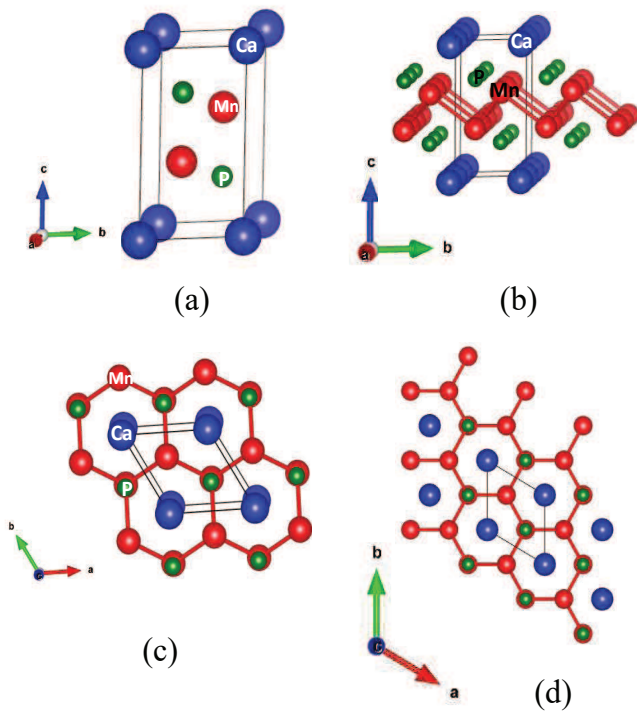


FIG. 2. Crystal structure of CaMn_2P_2 . (a) One unit cell of the trigonal structure. The Mn atoms are represented by filled red spheres, the phosphorus atoms by smaller filled green spheres, and the Ca atoms by larger filled blue spheres. (b) Projection of the structure on the b - c plane (of the hexagonal unit cell), showing the corrugated nature of the Mn honeycomb sublattice. (c,d) Projections of the lattice onto the a - b plane, emphasizing the projected corrugated honeycomb Mn sublattice.

We fitted the respective $\rho(T)$ data over restricted temperature intervals by

$$\log_{10} \rho = A + 2.303 \left(\frac{\Delta}{k_B T} \right), \quad (2)$$

where A is a constant, k_B is Boltzmann's constant, and Δ is the activation energy.

Plots of $\log_{10} \rho$ vs $1/T$ are shown in the insets of Figs. 3(a) and 3(b) for SrMn_2P_2 and CaMn_2P_2 , respectively. For SrMn_2P_2 , the high- T data between ≈ 270 K and 400 K are nearly linear in $1/T$ and were fitted by Eq. (2), yielding the intrinsic activation energy $\Delta = 0.124(3)$ eV as shown by the solid straight line in the inset of Fig. 3(a), and the extrapolations as dashed lines. The fitted activation energy is of the same order as found previously for isostructural BaMn_2Sb_2 [17]. However, the value here is much larger than the activation energy found for polycrystalline SrMn_2P_2 over the temperature range 200–300 K, which was 0.0129(2) eV [11].

For CaMn_2P_2 , the data between 220 K and 300 K and between 197 K and 164 K were respectively nearly linear in $1/T$ and were fitted by Eq (2), yielding the intrinsic activation energy at high T as $\Delta = 0.088(1)$ eV, whereas the extrinsic activation energy at low T is

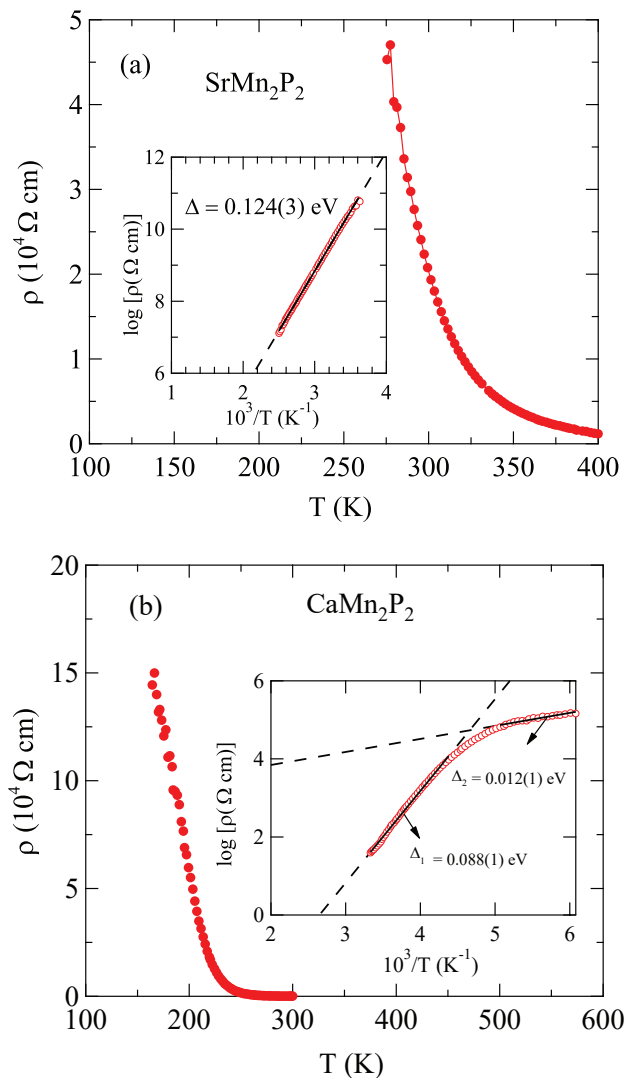


FIG. 3. Temperature T dependence of the electrical resistivity, $\rho(T)$, in the ab plane for (a) SrMn_2P_2 and (b) CaMn_2P_2 . The insets show plots of $\log_{10} \rho$ versus $1/T$. The solid straight lines through the inset data are fits over restricted temperature intervals by Eq. (2) as discussed in the text, and the dashed lines are extrapolations.

$\Delta = 0.012(1)$ eV. The fits are shown in the inset of Fig. 3(b) as the solid straight lines and the extrapolations by dashed lines. For comparison, the high- T intrinsic activation energy reported recently for single-crystal CaMn_2P_2 from ab -plane $\rho(T)$ data was $\Delta = 0.040$ eV and the extrinsic low- T value was 0.00064 eV [10].

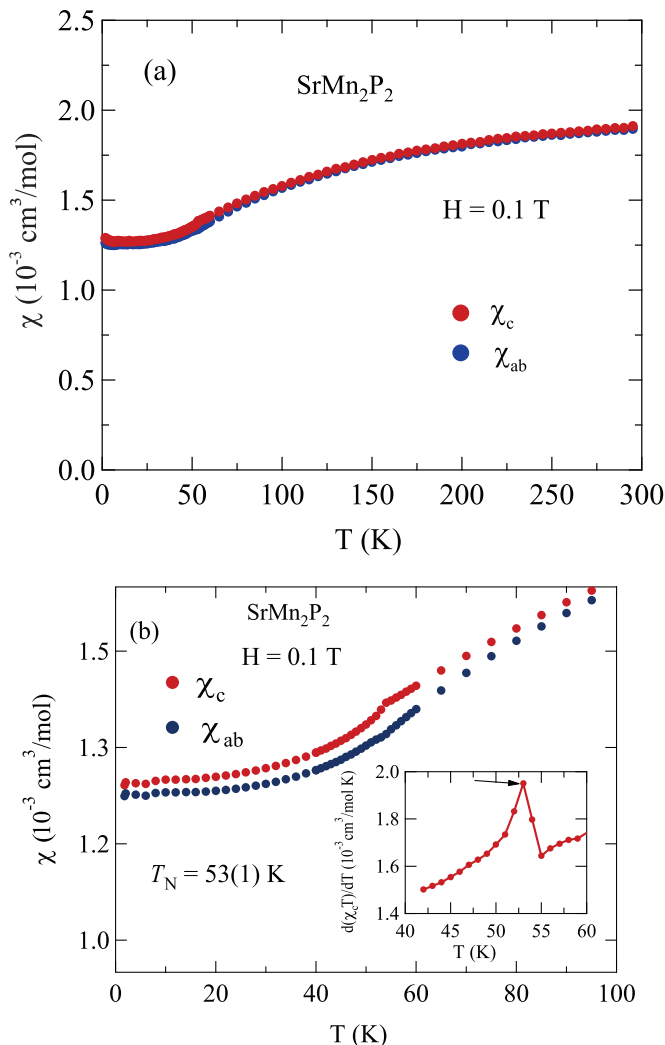


FIG. 4. (a) Temperature dependent zero-field-cooled magnetic susceptibility $\chi(T)$ of SrMn_2P_2 in a magnetic field $H = 0.1$ T applied in the ab plane (χ_{ab}) and along the c axis (χ_c). (b) The expanded plot of $\chi(T)$ between 1.8 and 100 K to highlight the transition. Inset: Derivative $d[\chi_c(T)]/dT$ versus T for $H \parallel c$, yielding $T_N = 53(1)$ K.

V. MAGNETIC SUSCEPTIBILITY AND MAGNETIZATION VERSUS FIELD ISOTHERMS

A. SrMn_2P_2

Figure 4(a) shows the zero-field-cooled (ZFC) magnetic susceptibility $\chi(T) \equiv M(T)/H$ of SrMn_2P_2 in a magnetic field $H = 0.1$ T applied in the ab plane (χ_{ab}) and along the c axis (χ_c). These data exhibit an AFM transition at $T_N = 53(1)$ K, clearly seen from the peak in the expanded plot of $d(\chi_c T)/dT$ versus T in Fig. 4(b) according to the Fisher relation [32]. The $\chi(T)$ below T_N is almost isotropic and the magnetic phase transition is sharper in $\chi_c(T)$. According to molecular field theory, the isotropic and nearly T -independent $\chi(T \leq T_N)$

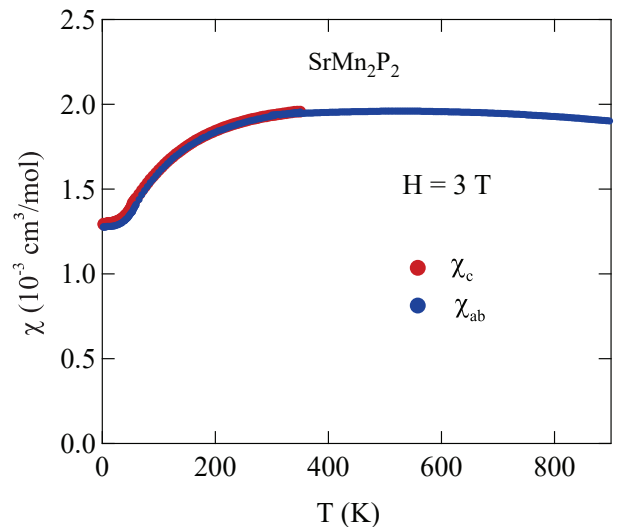


FIG. 5. Zero field cooled magnetic susceptibility χ_{ab} and χ_c versus T for $1.8 \text{ K} \leq T \leq 900 \text{ K}$ measured in $H = 3$ T.

suggests that the ordered moments form an AFM c -axis helix or ab -plane cycloidal structure with an approximately 120° turn angle, irrespective of the value of spin S [33, 34]. As will be shown below, ^{31}P NMR measurements suggest an incommensurate AFM state. Similar behaviors have been observed in 120° -ordered compounds such as VF_2 and VBr_2 [35]. The suggested magnetic structure in SrMn_2P_2 is different from the magnetic structure of the isostructural compound SrMn_2As_2 that was found to have a collinear AFM structure with the ordered moments aligned in the ab plane, but with three approximately equally populated domains at an angle of 120° from each other [16]; we found similar behavior in SrMn_2Sb_2 [17]. Neutron-diffraction measurements are needed confirm the magnetic structure in SrMn_2P_2 .

Figure 5 shows $\chi(T)$ of SrMn_2P_2 from 1.8 K to 900 K measured in $H = 3$ T. Unlike most local-moment antiferromagnets for which $\chi(T)$ decreases above T_N according to the Curie-Weiss law, the $\chi(T)$ above T_N in SrMn_2P_2 increases with T above T_N , exhibits a broad maximum at about 300 K and then slowly decreases. Therefore, the present data suggest that strong dynamic AFM fluctuations occur up to at least 900 K, similar to corresponding data for the isostructural compounds $(\text{Sr,Ca})\text{Mn}_2(\text{As,Sb})_2$ [15, 17]. Within a local-moment picture, these features at $T > T_N$ are characteristic of a quasi-one- or -two-dimensional antiferromagnet. Similar results were obtained for a polycrystalline sample of SrMn_2P_2 [11, 36].

$M(H)$ isotherms for a single crystal of SrMn_2P_2 with $H \parallel ab$ and $H \parallel c$ are shown in Figs. 6(a) and 6(b), respectively. The data for M_{ab} and M_c are proportional to H at all temperatures, indicating the absence of significant ferromagnetic or saturable paramagnetic impurities. The nearly isotropic $M(H, T < T_N)$ data for both

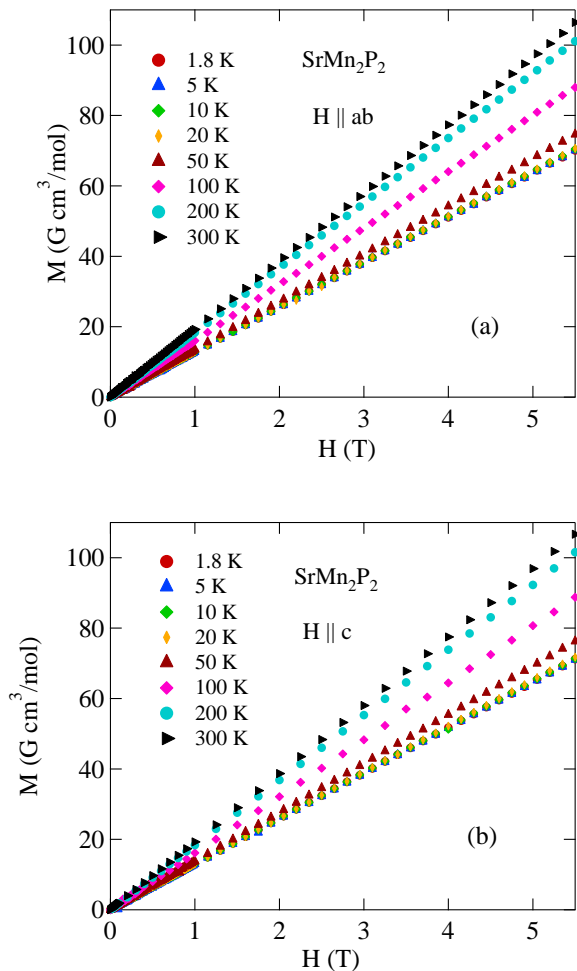


FIG. 6. Magnetization M of SrMn_2P_2 as a function of magnetic field H at various temperatures T with (a) H in the ab plane ($H \parallel ab$) and (b) H along c axis ($H \parallel c$).

field directions are consistent with the nearly isotropic behavior of $\chi(T)$ in Fig. 4(a).

We obtain an estimate of the exchange interactions between the Mn spins-5/2 in SrMn_2P_2 as follows. We assume that all spins are identical and crystallographically equivalent as in CaMn_2P_2 and SrMn_2P_2 . Within a local-moment Heisenberg picture, molecular-field theory predicts a magnetic susceptibility

$$\chi = \frac{C}{T - \theta_p}, \quad (3a)$$

where C is the Curie constant per mole of spins given by

$$C = \frac{N_A g^2 S(S+1)}{3k_B}, \quad (3b)$$

N_A is Avogadro's number, g is the spectroscopic splitting factor of a spin, and k_B is Boltzmann's constant. The

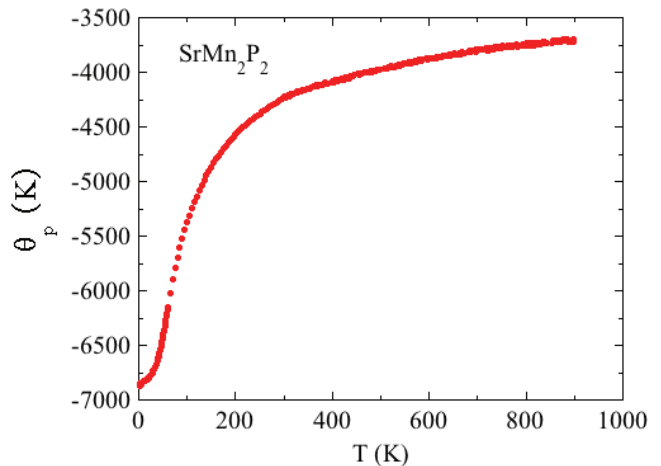


FIG. 7. Weiss temperature θ_p versus temperature T obtained using Eq. (6) and the $\chi_{ab}(T)$ data in Fig. 5.

paramagnetic Weiss temperature θ_p is given by [34]

$$\theta_p = -\frac{S(S+1)}{3k_B} \sum_j J_{ij}, \quad (3c)$$

which contains the sum of the Heisenberg exchange interactions J_{ij} between a central spin i and its neighbors j with which it interacts and an AFM J is positive. Here, because a formula unit of SrMn_2P_2 contains two magnetic Mn atoms, and if C is expressed in cgs units of $\text{cm}^3\text{-K}$ per mole of formula units, we get

$$C_{\text{f.u.}} = \frac{2N_A g^2 S(S+1)}{3k_B}. \quad (4)$$

Then using $g = 2$ and $S = 5/2$ gives

$$C_{\text{f.u.}} = 8.75 \frac{\text{cm}^3 \text{K}}{\text{molf.u.}}. \quad (5)$$

It is clear From Fig. 5 that $\chi_{ab}(T)$ does not attain Curie-Weiss behavior up to 900 K. However, if we calculate a T -dependent θ_p from Eq. (3a) given by

$$\theta_p(T) = T - \frac{C_{\text{f.u.}}}{\chi(T)}, \quad (6)$$

where $\chi(T) = \chi_{ab}(T)$ is the magnetic susceptibility per mole of formula units as in Fig. 5, we expect $\theta_p(T)$ to asymptote to its actual value θ_p as the dynamic short-range correlations diminish with increasing T .

Figure 7 shows a plot of θ_p versus T obtained from the data in Fig. 5 using Eq. (6). The data appear to asymptote at high temperatures to a value

$$\theta_p \sim -3500 \text{ K}, \quad (7)$$

where the negative sign indicates AFM interactions. Then using Eqs. (3c) and (7) we obtain

$$\sum_j J_{ij} = -\frac{3k_B \theta_p}{S(S+1)} \sim 0.10 \text{ eV}. \quad (8)$$

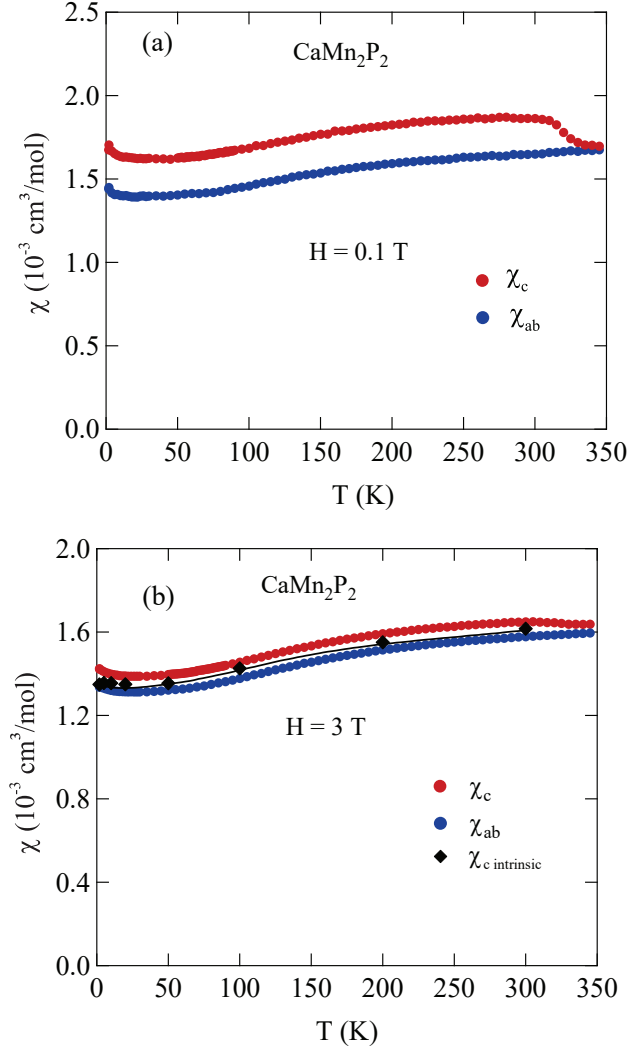


FIG. 8. Temperature dependent zero-field-cooled magnetic susceptibility $\chi(T)$ of CaMn_2P_2 in magnetic fields (a) $H = 0.1$ T, and (b) $H = 3$ T applied in the ab plane (χ_{ab}) and along the c axis (χ_c). In (b), the intrinsic $\chi_c(T)$ data obtained from the high-field slope of $M(H)$ isotherms are also included, denoted as $\chi_{c \text{ intrinsic}}$. In (a), the increase in the $\chi_c(T)$ data on cooling below 350 K is inferred to arise from a small amount of ferromagnetic MnP impurity, whereas in (b) the impurity magnetization is not as evident in the 3 T field.

If it is assumed that a given Mn spin only interacts with its three nearest neighbors in the corrugated honeycomb lattice with exchange interaction J , then $J \sim 34$ meV.

B. CaMn_2P_2

The zero-field-cooled (ZFC) magnetic susceptibilities $\chi \equiv M/H$ versus T measured in $H = 0.1$ T and $H = 3$ T applied in the ab plane ($H \parallel ab$, χ_{ab}) and along the c axis ($H \parallel c$, χ_c) for a single crystal of CaMn_2P_2 are shown

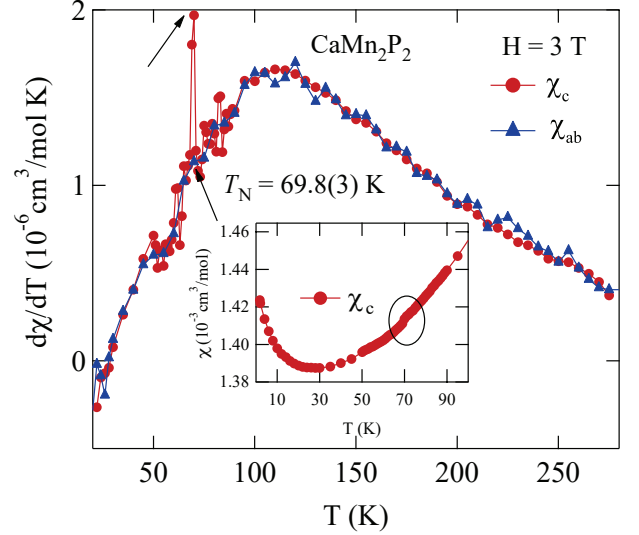


FIG. 9. Temperature derivative of the magnetic susceptibility $d\chi(T)/dT$ of CaMn_2P_2 in a magnetic field $H = 3$ T applied in the ab plane and along the c axis. Inset: Expanded plot of $\chi_c(T)$ to highlight the first-order AFM transition at $T_N = 69.8(3)$ K.

in Figs. 8(a) and 8(b), respectively. At first glance, there is no clear feature of any magnetic phase transition up to 350 K. However, an expanded plot of the $\chi_c(T)$ data in the inset of Fig. 9 shows a first-order AFM transition at ≈ 69 K. The temperature derivative of $\chi(T)$ versus T is plotted for both χ_{ab} and χ_c in Fig. 9, where the first-order nature of the magnetic transition in $\chi_c(T)$ is evident, which yields the more precise $T_N = 69.8(3)$ K. Contrary to our findings, Ref. [10] found that CaMn_2P_2 does not show any long-range magnetic ordering below 400 K. Instead, they found a first-order structural transition at $T^* = 69$ K from electrical resistivity and heat-capacity measurements and also found that T^* increases with increasing pressure. From the nearly isotropic $\chi(T)$ below T_N in Fig. 8(b), we suggest that the AFM structure is, or is similar to, a 120° c -axis helix or ab -plane cycloid [33, 34].

Like SrMn_2P_2 , CaMn_2P_2 is a low-dimensional antiferromagnet as seen by the very broad apparent maximum in $\chi(T)$ above T_N in Fig. 8(b). Indeed the Curie-Weiss temperature region of χ is not reached up to 350 K, indicating that strong AFM correlations survive to significantly higher temperatures than plotted. Previous studies of Mn pnictides suggested that for the d^5 electronic configuration of Mn^{2+} ($S = 5/2$) in trigonal Mn pnictides, the nearest-neighbor interactions are very strong and these compounds tended to have AFM correlations or develop long-range AFM order due to the competition among different exchange interactions between the Mn sites [2, 5, 15, 17].

In addition, a small upturn in $\chi_c(T)$ is seen in Fig. 8(a) below about 300 K. This is likely due to FM MnP impu-

urities with Curie temperature $T_c = 291.5$ K [37] that are present on the crystal surface and/or as an inclusion in the crystal, similar to BaMn_2As_2 [2] and SrMn_2As_2 [15] crystals with MnAs impurities. From a comparison of Figs. 8(a) and 8(b), this FM MnP impurity is most clearly seen in the $\chi_c(T)$ data with $H = 0.1$ T. In addition there is a small upturn in $\chi(T)$ data below ≈ 40 K which is likely due to the contribution of paramagnetic impurities.

Figures 10(a) and 10(b) show $M(H)$ isotherms for CaMn_2P_2 with H in the ab plane and along the c axis, respectively. The $M(H)$ data are almost linear for each temperature indicating that the amount of ferromagnetic seen in Fig. 8(a) is very small. The intrinsic magnetic behavior of χ_c data were extracted and for which the $M_c(H)$ data in the high-field range $H = 3.5$ – 5.5 T is fitted by the linear relation

$$M(H, T) = M_{\text{sat}}(T) + \chi_{\text{int}}(T)H, \quad (9)$$

where $M_{\text{sat}}(T)$ is the saturation magnetization due to the FM impurities. The $T \rightarrow 0$ value of M_{sat} for CaMn_2P_2 is $2 \text{ G cm}^3/\text{mol} = 0.00036 \mu_{\text{B}}/\text{f.u.}$, which corresponds to $0.03 \text{ mol}\%$ of MnP impurities using the saturation moment $\approx 1.33 \mu_{\text{B}}/\text{f.u.}$ [37] for MnP. The $\chi(T) \equiv M(T)/H$ data in Fig. 8(b) were measured with $H = 3$ T. Therefore, we obtained the intrinsic χ from the isotherm data according to

$$\chi_{\text{intrinsic}}(T) = \frac{M_{\text{measured}}(T) - M_{\text{sat}}(T)}{3 \text{ T}}. \quad (10)$$

The $\chi_{\text{intrinsic}}(T)$ data are shown by the filled black squares in Fig. 8(b) and the black solid line is a guide to eye. It is seen that the $\chi_{\text{intrinsic}}(T)$ data for CaMn_2P_2 follows the behavior of χ_{ab} , which means that there is no intrinsic anisotropy between the ab -plane and c -axis magnetization data, similar to SrMn_2P_2 as seen in the previous section.

VI. HEAT CAPACITY

Figures 11(a) and 11(b) show zero-field $C_p(T)$ data for SrMn_2P_2 and CaMn_2P_2 , respectively. The sharp peaks in $C_p(T)$ at 53 K in SrMn_2P_2 and at 69.8 K in CaMn_2P_2 are at the respective Néel temperatures of the two compounds found from the above $\chi(T)$ data. The $C_p(T)$ value obtained at 300 K is smaller than the classical Dulong-Petit limit of $3nR \sim 124 \text{ J/mol}\cdot\text{K}$ for both compounds and similar to that reported in Ref. [10] for CaMn_2P_2 . Figures 5 and 8 demonstrate that strong dynamic short-range AFM correlations persist up to high temperatures, as was previously found for the isostructural compounds CaMn_2As_2 and SrMn_2As_2 [15]. Thus extraction of the T -dependent lattice contribution to the heat capacity below 300 K which could then reveal the T dependence of the magnetic contribution is not possible with the information available.

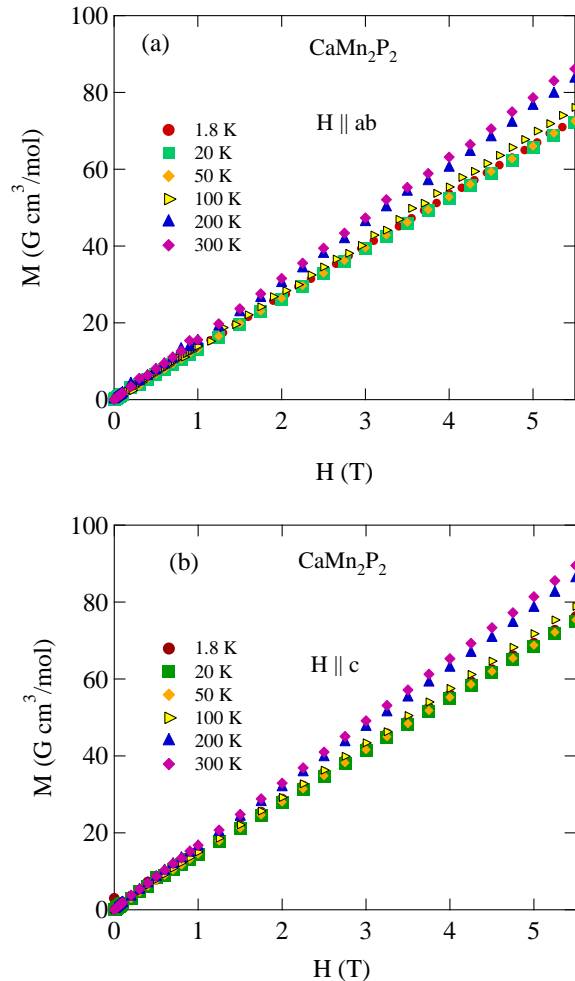


FIG. 10. Magnetization M of CaMn_2P_2 as a function of magnetic field H at various temperatures T with (a) H in the ab plane ($H \parallel ab$ plane) and (b) H along the c axis ($H \parallel c$).

The insets of Figs. 11(a) and 11(b) show $C_p(T)/T$ versus T^2 between 1.8 and 5 K. The data were fitted by

$$\frac{C_p}{T} = \beta T^2 \quad (11)$$

appropriate to insulators, where β reflects the low- T lattice contribution which we assume does not contain a three-dimensional AFM spin-wave contribution. From the fits of Eq. (11) to the data in the insets of Figs. 11(a) and 11(b), we obtain $\beta = 0.273(1) \text{ mJ}/(\text{mol K}^4)$ for SrMn_2P_2 and $0.262(1) \text{ mJ}/(\text{mol K}^4)$ for CaMn_2P_2 . The Debye temperature θ_D is given by

$$\theta_D = \left(\frac{12\pi^4 R n}{5\beta} \right)^{1/3}, \quad (12)$$

where R is the molar gas constant and n is the number of atoms per formula unit [$n = 5$ for $(\text{Sr or Ca})\text{Mn}_2\text{P}_2$]. Using the above β values we obtain $\theta_D = 329(3) \text{ K}$ and $314(1) \text{ K}$ for SrMn_2P_2 and CaMn_2P_2 , respectively.

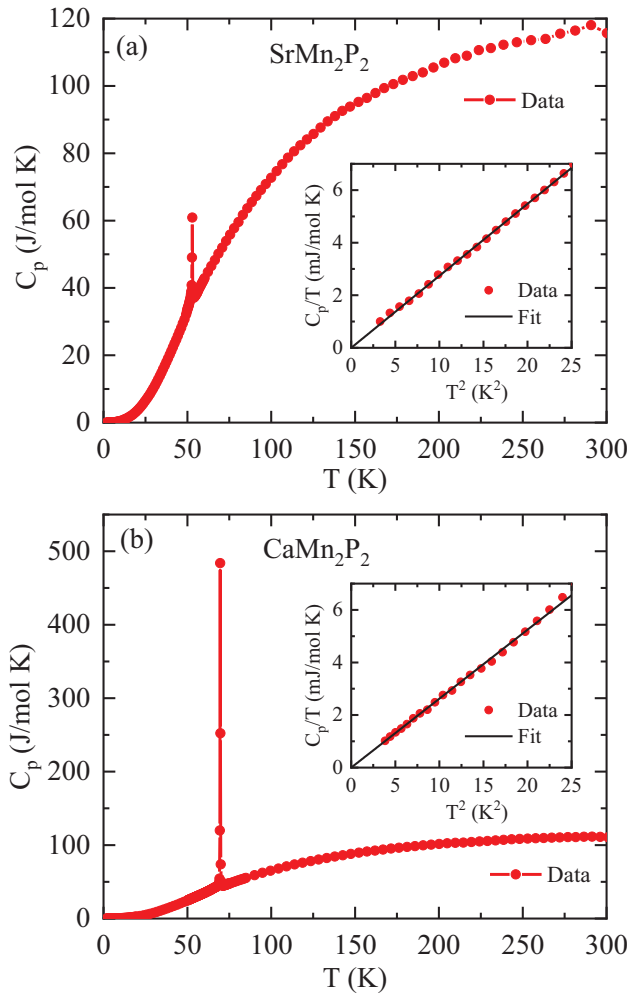


FIG. 11. Heat capacity C_p versus temperature T for (a) SrMn_2P_2 and (b) CaMn_2P_2 single crystals. Data near T_N were obtained using the single-pulse slope-analysis method. Insets: $C_p(T)/T$ versus T^2 for $T \leq 5$ K, where the straight lines through the respective data are fits by Eq. (11).

As seen in Figs. 11(a) and 11(b), in both compounds the experimentally-observed heat-capacity peak at T_N is very sharp, indicating weak and strong first-order transitions in SrMn_2P_2 and CaMn_2P_2 , respectively. Near T_N , the respective data were obtained utilizing the single-pulse slope-analysis method with heating curves as discussed in Section II. Figures 12(a) and 12(b) compare the conventionally-measured and slope-analyzed $C_p(T)$ data close to the first-order magnetic transition (FOMT) region of SrMn_2P_2 and CaMn_2P_2 , respectively. The slope-analyzed data show higher peak values than the conventionally-measured data.

For both compounds, the peak values of $C_p(T)$ obtained from the conventional measurement technique are seen from Fig. 12 to be about a factor of two smaller than those from the slope-analyzed data. From the latter data, the height of the C_p peak for SrMn_2P_2 above background is about 40 J/mol K, whereas that for CaMn_2P_2

is about 1000 J/mol K, indicating a much larger latent heat in CaMn_2P_2 . This difference is clearly visible in the temperature-response versus time $T(t)$ plots around the the respective FOMT for SrMn_2P_2 and CaMn_2P_2 as shown in Figs. 12(c) and 12(d), respectively. For a FOMT, the $T(t)$ curve exhibits a plateau at the transition temperature associated with the latent heat, as clearly observed for CaMn_2P_2 at T_N . Such a plateau is replaced by a region of negative curvature for SrMn_2P_2 indicating a much smaller latent heat associated with the FOMT for SrMn_2P_2 .

The latent heat Q associated with the FOMT for both compounds was calculated by first subtracting the respective $C_p(T)$ backgrounds using a polynomial fit and then measuring the area under the resultant peak. For SrMn_2P_2 we obtained $Q \approx 8.7$ J/mol at $T_N \approx 53$ K, whereas for CaMn_2P_2 we obtained $Q \approx 152$ J/mol at $T_N = 69.5$ K. The difference in the latent heat estimated from the conventionally-measured data and the slope-analyzed data is negligible for SrMn_2P_2 and is only ~ 11 J/mol for CaMn_2P_2 as shown in the insets of Figs. 12(a) and 12(b), respectively. The heat-capacity peak value in CaMn_2P_2 obtained from the slope-analyzed measurements is larger than obtained previously [10]. As shown in Figs. 12(e) and 12(f), an applied field $H = 9$ T has negligible influence on $C_p(T \approx T_N)$ for both SrMn_2P_2 and CaMn_2P_2 , respectively.

VII. NUCLEAR MAGNETIC RESONANCE

A. SrMn_2P_2

1. ^{31}P NMR spectrum

Figure 13(a) shows the typical T dependence of ^{31}P NMR spectra above T_N for $H \parallel ab$ plane (black lines) and $H \parallel c$ axis (red lines). For each magnetic field direction, we observed a single line as expected for the nuclear spin $I = 1/2$ NMR spectrum. However, although the NMR line is relatively sharp at high T , the spectra show asymmetric shapes. Since we used a single crystal for our measurements, the asymmetric shape indicates a slight distribution of the hyperfine field at the P sites and/or the presence of more than two P sites. Since only one P site is expected from the crystal structure, the origin of the asymmetric shape of the spectra is not clear at present.

Figure 13(b) shows the T dependence of the NMR shift for $H \parallel c$ axis (K_c) and $H \parallel ab$ plane (K_{ab}) determined by the peak position for each spectrum. Both K_c and K_{ab} decrease with decreasing T as in the case of the aforementioned magnetic susceptibility. The NMR shift has contributions from the T -dependent spin part K_{spin} and a T -independent orbital part K_0 . K_{spin} is proportional to the spin susceptibility χ_{spin} through the hyperfine coupling constant A giving $K(T) = K_0 + \frac{A}{N_A} \chi_{\text{spin}}(T)$, where

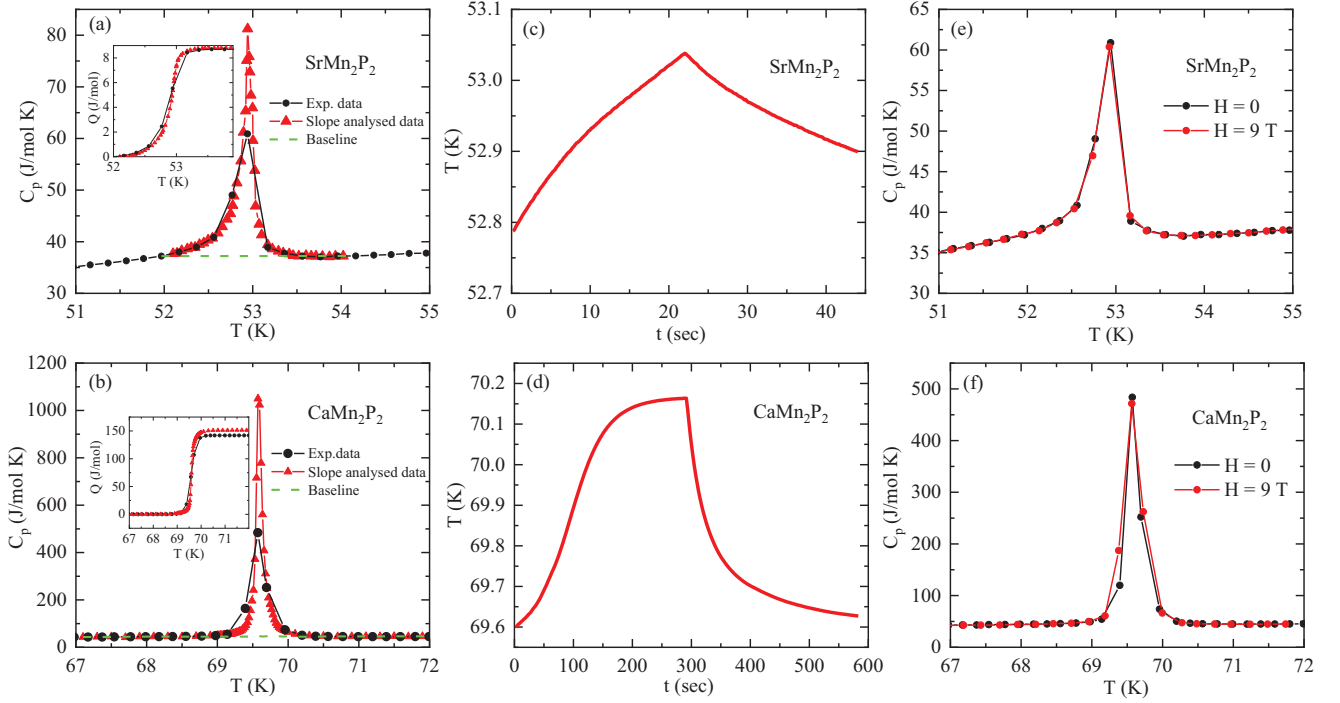


FIG. 12. Comparison of as-measured $C_p(T)$ data and the single-pulse slope-analysed data (using a heating curve) for (a) SrMn_2P_2 and (b) CaMn_2P_2 crystals. Insets: the latent heat associated with the first-order magnetic transition (FOMT). The $C_p(T)$ values at the FOMT are estimated by subtracting the polynomial-fitted baseline data (dashed green line) from the total $C_p(T)$ data in that temperature region as shown in (a) and (b). The temperature-response curve $T(t)$ at the FOMT for (c) SrMn_2P_2 and (d) CaMn_2P_2 . The conventionally-measured $C_p(T)$ is plotted for (e) SrMn_2P_2 and (f) CaMn_2P_2 with c -axis applied magnetic fields $H = 0$ and 9 T, respectively.

N_A is Avogadro's number. Figure 13(c) plots K_{ab} and K_c against χ_{ab} and χ_c , respectively, with T as an implicit parameter. Here we use the magnetic susceptibilities measured at $H = 3$ T. K_{ab} and K_c vary with the respective χ as expected, although one can see a slight deviation from the linear relationship for $H \parallel c$. The deviation could be due to the broadening of the spectrum below 100 K for $H \parallel c$.

We estimated the hyperfine coupling constants $A_c = (7.0 \pm 0.1)$ kOe/ μ_B and $A_{ab} = (4.4 \pm 0.1)$ kOe/ μ_B by fitting the data in Fig. 13(c) above 100 K. From the estimated hyperfine coupling constants, we evaluated the isotropic hyperfine coupling constant $A_{\text{iso}} = (5.23 \pm 0.10)$ kOe/ μ_B and the axially-anisotropic hyperfine coupling constant $A_{\text{ax}} = (0.9 \pm 0.1)$ kOe/ μ_B , respectively, from the relations $A_{\text{iso}} = (A_c + 2A_{ab})/3$ and $A_{\text{ax}} = (A_c - A_{ab})/3$. The A_{iso} originates from the transferred hyperfine interactions between the ^{31}P nucleus and its neighboring Mn^{2+} ions through the mixing of the Mn 3d and P 2s orbitals and/or polarization of inner-core s electrons via the P 2p orbitals. On the other hand, the A_{ax} part comes from the dipolar interactions from the Mn^{2+} spins at the P site and/or on-site dipolar field from the polarization of P 2p orbitals. It is noted that the hyperfine coupling constant at the P site is dominated by the isotropic part, although there is a $\sim 17\%$ contribution of the axially component with respect to the

isotropic part.

When T is lowered close to $T_N \approx 53$ K, as shown in Fig. 14(a) for $H \parallel ab$, a single sharp NMR line (denoted by P_{HT} in the figure) suddenly broadens due to the internal field (H_{int}) at the P site produced by the Mn^{2+} ordered moments in the AFM state. The observed spectra become nearly independent of T below 40 K as shown in Fig. 14(b), where the two peak positions denoted by P1 (H_{P1}) and P2 (H_{P2}) in Fig. 14(a) are plotted versus T .

The internal field H_{int} , which is proportional to the Mn^{2+} sublattice magnetization, was determined as half of the separation between P1 and P2. The temperature dependences of H_{int} are shown in Fig. 14(c) from which we estimated the critical exponent of the order parameter (sublattice magnetization). H_{int} was fitted by the power law $H_{\text{int}} = H_{\text{int},0}(1 - T/T_N)^\beta$ with $T_N = 53.0$ K. The solid line in the figure shows the curve with $H_{\text{int},0} = 0.175$ T and $\beta = 0.13$. Here the value of β is much smaller than expected for any three-dimensional magnetic material with a second-order phase transition such as $\beta = 0.33\text{--}0.367$ for 3D Heisenberg, $0.31\text{--}0.345$ for 3D XY, and $0.31\text{--}0.326$ for 3D Ising models [38], but close to 0.125 for the 2D Ising model [38]. These results suggest a second-order phase transition. In addition, we were able to follow the reduction in H_{int} near T_N and also detected a critical-slowing-down behavior in the T dependence of $1/T_1$ around T_N (shown below). Therefore, the magnetic

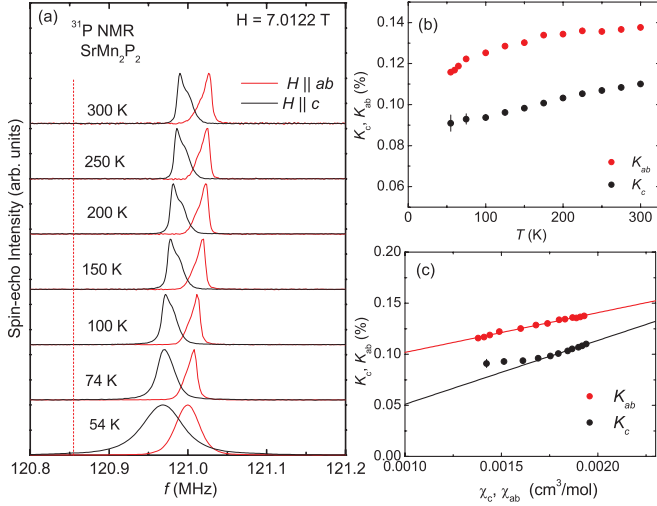


FIG. 13. (a) ^{31}P -NMR spectra under a magnetic field $H \sim 7.0122$ T parallel to the c axis (black) and parallel to the ab plane (red) at various temperatures in SrMn_2P_2 . The vertical dashed line represents the zero-shift position ($K = 0$). (b) Temperature dependence of the ^{31}P -NMR shifts K_c and K_{ab} . (c) χ plots for each magnetic field direction. The lines are fitting results.

phase transition for SrMn_2P_2 is considered to be characterized as a second-order phase transition. However, the above $C_p(T)$ data suggest a weak first-order transition, so the transition at T_N has characteristics of both orders of the transition. On the other hand, we will show below that CaMn_2P_2 exhibits a strong first-order phase transition where we observed a clear jump in the order parameter just below the magnetic phase transition temperature and also no observation of critical slowing down in T_1 measurements, in contrast to our observations for SrMn_2P_2 .

The broad NMR spectra observed below T_N indicate a distribution of internal fields H_{int} which is reminiscent of a two-horn structure expected for an incommensurate helical structure, as has been observed in EuCo_2P_2 [39] and EuCo_2As_2 [40]. In fact, the observed spectrum is reasonably reproduced by that calculated for an incommensurate helical AFM state shown by the green area assuming an internal field along the ab plane $H_{\text{int},ab} = 2.0$ kOe, although we note that one needs to introduce another P site with a smaller $H_{\text{int},ab} = 0.5$ kOe (shown by the light red area). The red curve is the sum of the two calculated spectra. The origin of the two P sites is not clear at present; however, it seems to be consistent with the observed ^{31}P NMR asymmetric spectra in the PM state which suggests that there is more than one P site having a different hyperfine coupling constant in the system. It is also noted that we consider only the isotropic hyperfine field for the calculation for simplicity; therefore, the slight deviation between the calculated and observed spectra could be due to the axially anisotropic part of the hyperfine field.

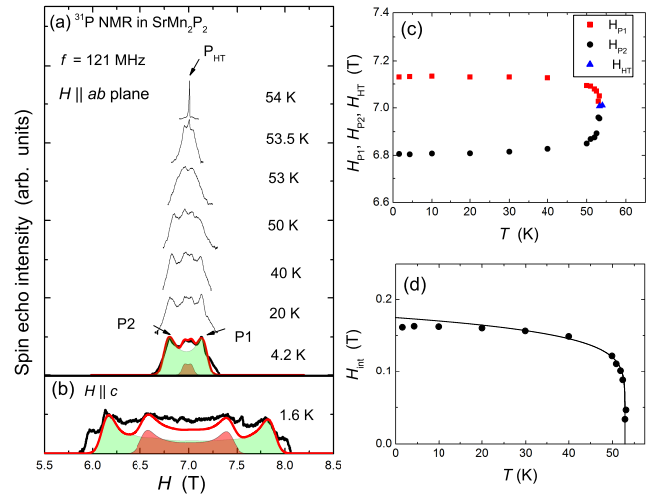


FIG. 14. (a) Field-swept ^{31}P -NMR spectra at a resonance frequency of $f = 121$ MHz for H parallel to the ab plane at various temperatures in SrMn_2P_2 below T_N . The black curves are the observed spectrum. The green and light-red areas are calculated spectra with an incommensurate helical AFM state with different internal fields of $H_{\text{int}} = 2.0$ and 0.5 kOe, respectively. The red curve is the sum of the two calculated spectra. (b) Field-swept ^{31}P -NMR spectrum at 1.6 K for $H \parallel c$. The black curves are the observed spectra and the other colored areas and line are the same with different internal fields (see text). (c) Temperature dependence of the peak positions for P_{HT} , P_1 and P_2 defined in (a). (d) Temperature dependence of $H_{\text{int}} = (H_{P_1} - H_{P_2})/2$. The solid line is the calculated result of $H_{\text{int}} = H_{\text{int},0}(1 - T/T_N)^\beta$ with $H_{\text{int},0} = 0.175$ T, $\beta = 0.13$ and $T_N = 53.0$ K.

A similar, but much broader, two-horn-like spectrum was observed for $H \parallel c$ in the AFM state as shown in Fig. 14(b). Here we were able to measure the spectrum only at 1.6 K and not at higher T due to poor signal intensity. The observed spectrum was also reasonably reproduced by a calculated spectrum for the incommensurate AFM state where again we assumed two different P sites with different internal fields along the c axis [$H_{\text{int},c} = 8.5$ kOe (green area), and $H_{\text{int},c} = 4.5$ kOe (light red area)]. As for $H \parallel ab$, the observed spectrum was not perfectly reproduced by the calculated spectrum. However, we consider that the analysis captures the essential point, evidencing the incommensurate AFM state in SrMn_2P_2 .

Our NMR results are consistent with previous $\chi(T)$ data for a polycrystalline SrMn_2P_2 sample and associated powder neutron-diffraction data [36] that suggested the presence of a complex low-dimensional [41] incommensurate AFM structure of high-spin Mn^{2+} below $T_N = 52(2)$ K with significant short-range AFM order well above T_N .

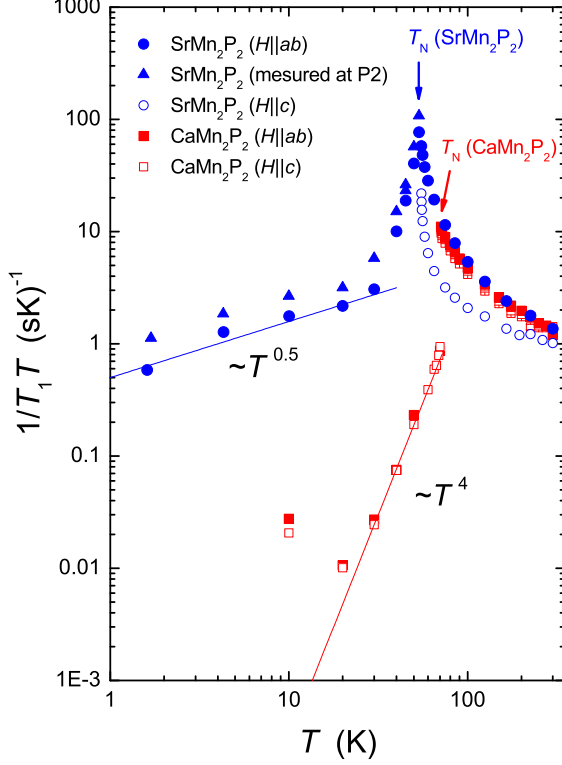


FIG. 15. Temperature dependence of $1/T_1T$ for SrMn_2P_2 and CaMn_2P_2 for both magnetic field directions, $H \parallel c$ axis and $H \parallel ab$ plane. The blue circles and triangles in the AFM state of SrMn_2P_2 for $H \parallel ab$ are the results measured at nearly zero-shift and the P2 positions, respectively. For the AFM state of CaMn_2P_2 , $1/T_1T$ was measured at the P3 position for $H \parallel c$ and at the lowest field peak for $H \parallel ab$. The blue and red straight lines show the power law dependences $1/T_1T \propto T^{-0.5}$ and T^4 , respectively.

2. ^{31}P spin-lattice relaxation rate $1/T_1$

Figure 15 shows the temperature dependence of the ^{31}P spin-lattice relaxation rate divided by temperature $1/T_1T$ for H parallel to the c axis and the ab plane. For $H \parallel ab$, $1/(T_1T)_{ab}$ was measured at the peak position for the spectra in the PM state and at nearly zero shift position of the spectra in the AFM state, while $1/(T_1T)_c$ for $H \parallel c$ was measured only in the PM state due to poor signal intensity in the AFM state.

As seen in the figure, with decreasing temperature, both $1/T_1T$ gradually increase and strongly enhance below ~ 60 K. For $H \parallel ab$, $1/T_1T$ starts to decrease just below $T_N = 53$ K, exhibiting a clear peak in $1/T_1T$ which is usually explained by a critical slowing down of spin fluctuations expected for a second-order phase transition. Thus our $1/T_1T$ data show the nature of the second-order phase transition for the AFM-PM transition in SrMn_2P_2 .

In order to discuss magnetic fluctuation effects in the

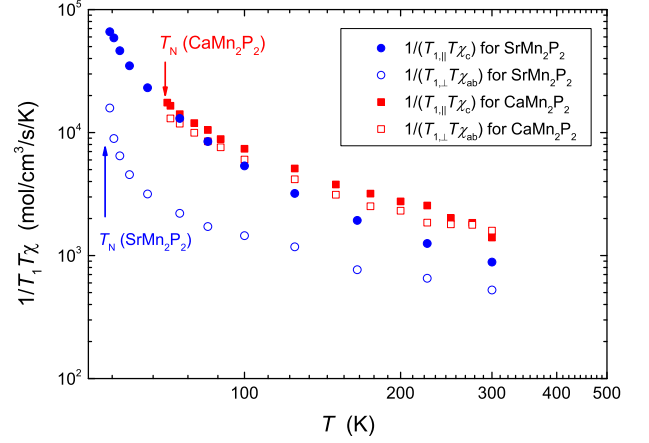


FIG. 16. Temperature dependence of $1/(T_{1,\perp}T\chi_{ab})$ and $1/(T_{1,\parallel}T\chi_c)$ for SrMn_2P_2 and CaMn_2P_2 .

PM state, it is useful to re-plot the $1/T_1$ data by changing the vertical axis from $1/T_1T$ to $1/T_1T\chi$ as shown in Fig. 16. In general, $1/T_1T$ can be expressed in terms of the imaginary part of the dynamic susceptibility $\chi''(\vec{q}, \omega_0)$ per mole of electronic spins as [42]

$$\frac{1}{T_1T} = \frac{2\gamma_N^2 k_B}{N_A^2} \sum_{\vec{q}} |A(\vec{q})|^2 \frac{\chi''(\vec{q}, \omega_0)}{\omega_0}, \quad (13)$$

where the sum is over the wave vectors \vec{q} within the first Brillouin zone, $A(\vec{q})$ is the form factor of the hyperfine interactions and $\chi''(\vec{q}, \omega_0)$ is the imaginary part of the dynamic susceptibility at the Larmor frequency ω_0 . On the other hand, the uniform χ corresponds to the real component $\chi'(\vec{q}, \omega_0)$ with $q = 0$ and $\omega_0 = 0$. Thus a plot of $1/T_1T\chi$ versus T shows the T dependence of $\sum_{\vec{q}} |A(\vec{q})|^2 \chi''(\vec{q}, \omega_0)$ compared to that of the uniform susceptibility $\chi'(0, 0)$. Since $1/T_1T$ probes magnetic fluctuations perpendicular to the magnetic field [42], we calculated $1/(T_{1,\perp}T\chi_{ab})$ using the relation $1/(T_{1,\perp}T) = 1/(T_1T)_c$, when examining the character of magnetic fluctuations in the ab plane. Similarly, we estimated $1/(T_{1,\parallel}T\chi_c)$ for magnetic fluctuations along the c axis from the relation [43]

$$1/(T_{1,\parallel}T) = 2/(T_1T)_{ab} - 1/(T_1T)_c. \quad (14)$$

As shown in Fig. 16, both $1/(T_{1,\perp}T\chi_{ab})$ and $1/(T_{1,\parallel}T\chi_c)$ increase with decreasing T . The results imply that $\sum_{\vec{q}} |A(\vec{q})|^2 \chi''(\vec{q}, \omega_0)$ increases more than $\chi'(0, 0)$, evidencing a growth of spin fluctuations with $q \neq 0$. Thus we conclude that AFM fluctuations exist in the PM state in SrMn_2P_2 . It is noted that the AFM fluctuations are more enhanced along the c axis than within the ab plane in SrMn_2P_2 . It is also interesting to point out that from the smooth extrapolation of the T dependence of both $1/(T_{1,\perp}T\chi_{ab})$ and $1/(T_{1,\parallel}T\chi_c)$, the AFM fluctuations seem to persist up to temperatures

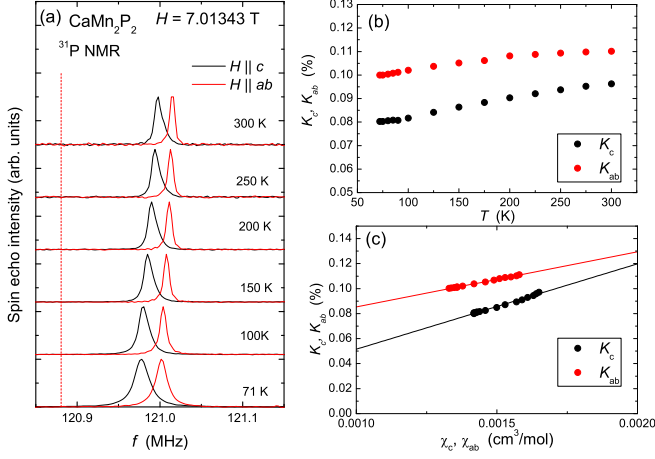


FIG. 17. (a) ^{31}P -NMR spectra under a magnetic field $H = 7.01343$ T parallel to the c axis (black) and parallel to the ab plane (red) at various temperatures in CaMn_2P_2 . The vertical dashed line represents the zero-shift position ($K = 0$). (b) Temperature dependence of the ^{31}P -NMR shifts K_c and K_{ab} . (c) K vs. χ plots for each field direction. The lines are fitting results.

much higher than 300 K, consistent with the $\chi(T)$ results discussed above.

In the AFM state below T_N , $1/T_1T$ for $H \parallel ab$ decreases slowly where $1/T_1T$ shows a $T^{0.5}$ power-law behavior. We also measured $1/T_1T$ in the AFM state at the lower field peak (P2) which shows similar power-law behavior with slightly different values (shown by the blue triangles in Fig. 15). In the AFM state, $1/T_1T$ is mainly driven by scattering of magnons, leading to T^2 and T^4 power-law T dependencies due to a two- or three-magnon Raman process, respectively [44]. The weak T dependence of $1/T_1T \propto T^{0.5}$ below 40 K cannot be explained by the magnon scattering, and suggests the presence of other magnetic fluctuations in the magnetically-ordered state.

B. CaMn_2P_2

1. ^{31}P NMR spectrum

Similar ^{31}P -NMR measurements were performed on CaMn_2P_2 . Figure 17(a) shows the typical T dependence of NMR spectra for $H \parallel ab$ and $H \parallel c$ in the PM state. As in the case of SrMn_2P_2 , a single NMR line was observed. The T dependencies of the NMR shifts are shown in Fig. 17(b), and Fig. 17(c) shows K - χ plots for both magnetic field directions. From the slopes in Fig. 17(c), the hyperfine coupling constants were estimated to be $A_c = (7.6 \pm 0.1) \text{ kOe}/\mu_B$ and $A_{ab} = (4.9 \pm 0.1) \text{ kOe}/\mu_B$ for $H \parallel c$ and $H \parallel ab$, respectively, leading to the isotropic hyperfine coupling constant $A_{\text{iso}} = (5.8 \pm 0.1) \text{ kOe}/\mu_B$ and the axially-anisotropic hyperfine coupling constant

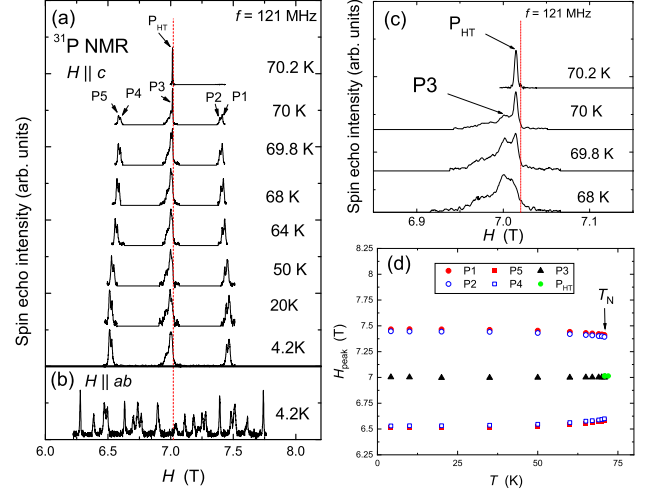


FIG. 18. (a) Field-swept ^{31}P -NMR spectra at a resonance frequency $f = 121$ MHz for $H \parallel c$ in CaMn_2P_2 at various T below T_N . (b) Field-swept ^{31}P -NMR spectrum at 4.2 K for $H \parallel ab$. (c) Expanded ^{31}P NMR spectra near the zero-shift position for temperatures near T_N . (d) Temperature dependence of the peak positions for P_{HT} and P1–P5 defined in (a).

$$A_{\text{ax}} = (0.9 \pm 0.1) \text{ kOe}/\mu_B.$$

Although the ^{31}P NMR spectra in the PM state and the values of the hyperfine coupling constants in CaMn_2P_2 are similar to those observed in SrMn_2P_2 , surprisingly, the ^{31}P NMR spectra in the AFM state below T_N are quite different from the case of SrMn_2P_2 . As shown in Fig. 18(a) for $H \parallel c$, the single NMR line observed in the PM state suddenly splits into mainly three lines at the higher and lower magnetic field positions with a double-peak structure (denoted by P1, P2, P4, and P5) and around a nearly zero-shift position (P3) in the AFM state. The detailed change in the NMR spectrum around zero-shift position are shown in Fig. 18(c). Note here we measured the spectrum with increasing T . No P_{HT} signal from the PM state could be observed and only the signal (P3) from the AFM state was detected at 68 K. Then, P_{HT} starts to appear at 69.8 K and the P3 signal disappears completely at 70.2 K. The coexistence of the two signals from the AFM and PM states can be seen in a quite narrow temperature range from 69.8 K to 70 K, indicating a very small hysteresis.

The distinct splittings of the NMR line below T_N clearly indicate that the AFM state is commensurate, which is in strong contrast to the case of the incommensurate AFM state in SrMn_2P_2 . Similar distinct splittings of NMR lines were also observed for $H \parallel ab$ where a more complicated spectrum with at least 20 peaks were detected [see, Fig. 18(b)]. Although the spectrum is complicated and suggests a complex magnetic structure, it is clear that the commensurate nature holds not only along the c axis but also in the ab plane.

Figure 18(d) shows the T dependence of the peak po-

sitions for $H \parallel c$. Clear jumps in the positions due to a finite internal field below T_N can be seen. These results clearly show that the AFM phase transition in CaMn_2P_2 is of first order, consistent with the results of the $C_p(T)$ measurements.

2. ^{31}P spin-lattice relaxation rate $1/T_1$

The clear nature of the first-order phase transition in CaMn_2P_2 can be also detected in the temperature dependence of $1/T_1T$. As shown in Fig. 15, in the PM state, $1/T_1T$ for $H \parallel c$ and $H \parallel ab$ gently increases with decreasing T with no obvious anisotropy. $1/T_1T$ for both magnetic field directions in CaMn_2P_2 does not exhibit a clear enhancement close at T_N , indicating no critical slowing down of the Mn spins as expected for the first-order phase transition. In addition, $1/T_1T$ shows a discontinuous decrease just below T_N , which again confirms the first-order nature of the AFM magnetic phase transition in CaMn_2P_2 .

The increases of $1/T_1T$ in the PM state are due to the growth of AFM fluctuations which persist to much higher temperatures above 300 K as in the case of SrMn_2P_2 . However, as shown in Fig. 16, $1/(T_{1,\perp}T\chi_{ab})$ and $1/(T_{1,\parallel}T\chi_c)$ are nearly the same which suggests nearly isotropic AFM fluctuations in the PM state of CaMn_2P_2 , in contrast to the case of SrMn_2P_2 .

In the AFM state, the $1/T_1T$ data shown in Fig. 15 were measured at the P3 position for $H \parallel c$ and at the lowest-field peak for $H \parallel ab$. We also measured $1/T_1T$ at different peak positions for both magnetic field directions and found no obvious difference in the values of $1/T_1T$. $1/T_1T$ for $H \parallel c$ and $H \parallel ab$ show T^4 power-law behaviors which are consistent with T^4 expected for the three-magnon relaxation process in AFM materials where the deviation from the power-law behavior for $T \lesssim 20$ K could be due to relaxation associated with impurities.

VIII. CONCLUDING REMARKS

Single crystals of SrMn_2P_2 and CaMn_2P_2 have been grown using Sn flux and characterized by single-crystal x-ray diffraction, electrical resistivity ρ , heat capacity C_p , and NMR measurements versus temperature T , and anisotropic magnetic susceptibility χ and magnetization M versus T and applied magnetic field H measurements. Room-temperature single-crystal x-ray diffraction measurements confirm that both SrMn_2P_2 and CaMn_2P_2 adopt the trigonal CaAl_2Si_2 -type structure containing corrugated honeycomb quasi-two-dimensional Mn spin lattices as previously reported. The $\rho(T)$ measurements demonstrate insulating ground states for both

compounds with intrinsic activation energies of 0.124 eV for SrMn_2P_2 and 0.088 eV for CaMn_2P_2 . The $\chi(H, T)$ and $C_p(T)$ measurements reveal first-order AFM transitions at $T_N = 53(1)$ K and $69.8(3)$ K for SrMn_2P_2 and CaMn_2P_2 , respectively.

Li and coworkers reported a first-order transition at 69.5 K at in CaMn_2P_2 from $C_p(T)$ and $\rho(T)$ measurements in 2020 [10] and from Raman scattering measurements inferred that it was related to a structural transition such as superstructure formation although its potential concomitant magnetic character was not identified.

First-order AFM transitions in $H = 0$ are rather unusual. A first-order magnetostructural transition was observed at $T_N = 205$ K in the body-centered-tetragonal metallic 122-type Fe-based pnictide SrFe_2As_2 which exhibits a transition to an orthorhombic structure with commensurate, collinear, itinerant, spin-density-wave order [45–48]. This is a different class of materials from CaMn_2P_2 and SrMn_2P_2 which are electrical insulators. The cubic pyrite-structure insulator MnS_2 containing Mn^{2+} cations with high-spin $S = 5/2$ and $(\text{S}_2)^{2-}$ species was found from neutron-diffraction measurements to exhibit a first-order AFM transition at $T_N = 47.7$ K [49, 50]. Other examples of materials exhibiting first-order AFM transitions include insulating UO_2 with $T_N = 30.8$ K [51] and MnO [52, 53] with $T_N \approx 120$ K, and Cr and Eu metals. The AFM structure in Cr metal below $T_N = 311$ K is an itinerant spin-density wave [54], whereas it is a $S = 7/2$ local-moment helical AFM state below $T_N \approx 90$ K in Eu metal [55–57].

In a series of papers, it was found that symmetry considerations and renormalization-group theory could determine whether or not a given material would exhibit a first-order transition at its Néel temperature [58–61]. The theory correctly predicted the occurrence of first-order transitions in the above materials UO_2 , MnO , Cr, and Eu at their respective Néel temperatures. It would be interesting to see if the same theory would predict the observed first-order AFM transitions in CaMn_2P_2 and SrMn_2P_2 . If not, then a structural transition at T_N would evidently be required to explain the observed first-order transitions. For example, a crystal-structure distortion at T_N was stated to result in a first-order AFM transition in GeNCr_3 [62].

ACKNOWLEDGMENTS

This research was supported by the U.S. Department of Energy, Office of Basic Energy Sciences, Division of Materials Sciences and Engineering. Ames Laboratory is operated for the U.S. Department of Energy by Iowa State University under Contract No. DE-AC02-07CH11358.

[1] J. An, A. S. Sefat, D. J. Singh, and M.-H. Du, Electronic structure and magnetism in BaMn_2As_2 and BaMn_2Sb_2 ,

- [2] Y. Singh, A. Ellern, and D. C. Johnston, Magnetic, transport and thermal properties of single crystals of the layered arsenide BaMn_2As_2 , *Phys. Rev. B* **79**, 094519 (2009).
- [3] D. C. Johnston, R. J. McQueeney, B. Lake, A. Honacker, M. E. Zhitomirsky, R. Nath, Y. Furukawa, V. P. Antropov, and Y. Singh, Magnetic exchange interactions in BaMn_2As_2 : A case study of the J_1 - J_2 - J_c Heisenberg model, *Phys. Rev. B* **84**, 094445 (2011).
- [4] E. Brechtel, G. Cordier, and H. Schäfer, Preparation and Crystal Structure of BaMn_2Sb_2 , BaZn_2Sb_2 and BaCd_2Sb_2 , *Z. Naturforsch.* **34b**, 921 (1979).
- [5] J. Zeng, S. Qin, C. Le, and J. Hu, Magnetism and superconductivity in the layered hexagonal transition metal pnictides, *Phys. Rev. B* **96**, 174506 (2017).
- [6] J. B. Fouet, P. Sindzingre, and C. Lhuillier, An investigation of the quantum J_1 - J_2 - J_3 model on the honeycomb lattice, *Eur. Phys. J. B* **20**, 241 (2001).
- [7] I. I. Mazin, CaMn_2Sb_2 : a fully frustrated classical magnetic system, arXiv:1309.3744.
- [8] J. W. Simonson, G. J. Smith, K. Post, M. Pezzoli, J. J. Kistner-Morris, D. E. McNally, J. E. Hassinger, C. S. Nelson, G. Kotliar, D. N. Basov, and M. C. Aronson, Magnetic and structural phase diagram of CaMn_2Sb_2 , *Phys. Rev. B* **86**, 184430 (2012).
- [9] D. E. McNally, J. W. Simonson, J. J. Kistner-Morris, G. J. Smith, J. E. Hassinger, L. DeBeer-Schmitt, A. I. Kolesnikov, I. A. Zalitznak, and M. C. Aronson, CaMn_2Sb_2 : Spin waves on a frustrated antiferromagnetic honeycomb lattice, *Phys. Rev. B* **91**, 180407(R) (2015).
- [10] Y. J. Li, F. Jin, Z. Y. Mi, J. Guo, W. Wu, Z. H. Yu, D. S. Wu, S. H. Na, C. Mu, X. B. Zhou, Z. Li, K. Liu, L. L. Sun, Q. M. Zhang, T. Xiang, G. Li, and J. L. Luo, First-order transition in trigonal structure CaMn_2P_2 , *Euro. Phys. Lett.* **132**, 46001 (2020).
- [11] S. L. Brock, J. E. Greedan, and S. M. Kauzlarich, Resistivity and magnetism of AMn_2P_2 ($A = \text{Sr}, \text{Ba}$): The effect of structure type on physical properties, *J. Solid State Chem.* **113**, 303 (1994).
- [12] W. Xie, M. J. Winiarski, T. Klimczuk and R. J. Cava, A tetragonal polymorph of SrMn_2P_2 made under high pressure—theory and experiment in harmony, *Dalton Trans.*, **46**, 6835 (2017).
- [13] A. Mewis, AB_2X_2 -Compounds with the CaAl_2Si_2 Structure, V[1] The Crystal Structure of CaMn_2P_2 , CaMn_2As_2 , SrMn_2P_2 , and SrMn_2As_2 , *Z. Naturforsch.* **33b**, 606 (1978).
- [14] M. E. Lines, Magnetism in Two Dimensions, *J. Appl. Phys.* **40**, 1352 (1969).
- [15] N. S. Sangeetha, A. Pandey, Z. A. Benson and D. C. Johnston, Strong magnetic correlations to 900 K in single crystals of the trigonal antiferromagnetic insulators SrMn_2As_2 and CaMn_2As_2 , *Phys. Rev. B* **94**, 094417 (2016).
- [16] P. Das, N. S. Sangeetha, A. Pandey, Z. A. Benson, T. W. Heitmann, D. C. Johnston, A. I. Goldman, and A. Kreyssig, Collinear antiferromagnetism in trigonal SrMn_2As_2 revealed by single-crystal neutron diffraction, *J. Phys.: Condens. Matter* **29**, 035802 (2017).
- [17] N. S. Sangeetha, V. Smetana, A.-V. Mudring, and D. C. Johnston, Antiferromagnetism in semiconducting SrMn_2Sb_2 and BaMn_2Sb_2 single crystals, *Phys. Rev. B* **97**, 014402 (2018).
- [18] S. Bobev, J. Merz, A. Lima, V. Fritsch, J. D. Thompson, J. L. Sarrao, M. Gillissen, and R. Dronskowski, Unusual Mn–Mn Spin Coupling in the Polar Intermetallic Compounds CaMn_2Sb_2 and SrMn_2Sb_2 , *Inorg. Chem.* **45**, 4047 (2006).
- [19] W. Ratchiff II, A. L. Lima Sharma, A. M. Gomes, J. L. Gonzalez, Q. Huang, and J. Singleton, The magnetic ground state of CaMn_2Sb_2 , *J. Magn. Magn. Mater.* **321**, 2612 (2009).
- [20] C. A. Bridges, V. V. Krishnamurthy, S. Poulton, M. P. Paranthaman, B. C. Sales, C. Myers, and S. Bobev, Magnetic order in CaMn_2Sb_2 studied via powder neutron diffraction, *J. Magn. Magn. Mater.* **321**, 3653 (2009).
- [21] Q. D. Gibson, H. Wu, T. Liang, M. N. Ali, N. P. Ong, Q. Huang, and R. J. Cava, Magnetic and electronic properties of CaMn_2Bi_2 : A possible hybridization gap semiconductor, *Phys. Rev. B* **91**, 085128 (2015).
- [22] S. Lee, S. Choi, J. Kim, H. Sim, C. Won, S. Lee, S. A. Kim, N. Hur, and J.-G. Park, Antiferromagnetic ordering in Li_2MnO_3 , *J. Phys.: Condens. Matter* **24**, 456004 (2012).
- [23] APEX3, Bruker AXS Inc., Madison, Wisconsin, USA, 2015.
- [24] SAINT, Bruker AXS Inc., Madison, Wisconsin, USA, 2015.
- [25] L. Krause, R. Herbst-Irmer, G. M. Sheldrick, and D. J. Stalke, Comparison of silver and molybdenum microfocus X-ray sources for single-crystal structure determination, *Appl. Crystallogr.* **48**, 3 (2015).
- [26] G. M. Sheldrick, SHELTX – Integrated space-group and crystal-structure determination, *Acta Crystallogr. A* **71**, 3 (2015).
- [27] G. M. Sheldrick, Crystal structure refinement with SHELXL, *Acta Crystallogr. C* **71**, 3 (2015).
- [28] V. Hardy, Y. Bréard and C. Martin, Derivation of the heat capacity anomaly at a first-order transition by using a semi-adiabatic relaxation technique, *J. Phys.: Condens. Matter* **21**, 075403 (2009).
- [29] H. Suzuki, A. Inaba, C. Meingast, Accurate heat capacity data at phase transitions from relaxation calorimetry, *Cryogenics* **50**, 693 (2010).
- [30] F. Guillou, A. K. Pathak, D. Paudyal, Y. Mudryk, F. Wilhelm, A. Rogalev, and V.K. Pecharsky, Non-hysteretic first-order phase transition with large latent heat and giant low-field magnetocaloric effect, *Nat. Commun.* **9**, 2925 (2018).
- [31] *PPMS Heat Capacity Option User's Manual, 1085-150, Rev. M7*, Quantum Design, December 2017.
- [32] M. E. Fisher, Relation between the specific heat and susceptibility of an antiferromagnet, *Phil. Mag.* **7**, 1731 (1962).
- [33] D. C. Johnston, Magnetic Susceptibility of Collinear and Noncollinear Heisenberg Antiferromagnets, *Phys. Rev. Lett.* **109**, 077201 (2012).
- [34] D. C. Johnston, Unified molecular field theory for collinear and noncollinear Heisenberg antiferromagnets, *Phys. Rev. B* **91**, 064427 (2015).
- [35] K. Hirakawa, H. Ikeda, H. Kadowaki, and K. Ubukoshi, *J. Phys. Soc. Jpn.* **52**, 2882 (1983).
- [36] S. L. Brock, J. E. Greedan, and S. M. Kauzlarich, A Test of the Application of Extended Hückel Calculations to the ThCr_2Si_2 and CaAl_2Si_2 Structure Types: the Case of SrMn_2P_2 and BaMn_2P_2 , *J. Solid State Chem.* **109**, 416 (1994).

- [37] H. Obara, Y. Endoh, Y. Ishikawa and T. Komatsubara, Magnetic Phase Transition of MnP under Magnetic Field, *J. Phys. Soc. Jpn.* **49**, 3 (1980).
- [38] R. Nath, Y. Furukawa, F. Borsa, E. E. Kaul, M. Baenitz, C. Geibel, and D. C. Johnston, Single-crystal ^{31}P NMR studies of the frustrated square-lattice compound $\text{Pb}_2(\text{VO})(\text{PO}_4)_2$, *Phys. Rev. B* **80**, 214430 (2009) and references therein.
- [39] N. Higa, Q.-P. Ding, M. Yogi, N. S. Sangeetha, M. Hedo, T. Nakama, Y. Ōnuki, D. C. Johnston, and Y. Furukawa, NMR studies of the incommensurate helical antiferromagnet EuCo_2P_2 : Determination of antiferromagnetic propagation vector, *Phys. Rev. B* **96**, 024405 (2017).
- [40] Q.-P. Ding, N. Higa, N. S. Sangeetha, D. C. Johnston, and Y. Furukawa, NMR determination of an incommensurate helical antiferromagnetic structure in EuCo_2As_2 , *Phys. Rev. B* **95**, 184404 (2017).
- [41] R. Navarro, J. J. Smit, L. J. de Jongh, W. J. Crama, and D. J. W. Ijdo, Experimental and Theoretical Study of the Antiferromagnetic Double-Layer Compounds $\text{Rb}_3\text{Mn}_2\text{F}_7$ and $\text{K}_3\text{Mn}_2\text{F}_7$, *Physica* **83B**, 97 (1976).
- [42] T. Moriya, The Effect of Electron-Electron Interaction on the Nuclear Spin Relaxation in Metals, *J. Phys. Soc. Jpn.* **18**, 516 (1963).
- [43] Strictly speaking, this simple relation can not be applicable if $1/T_1T$ has a strong anisotropy in the ab plane. For CaMn_2P_2 , similar values of $1/(T_1T)_c$ and $1/(T_1T)_{ab}$ suggest no strong anisotropy in $1/T_1T$ within the ab plane so that one can use the relation. In the case of SrMn_2P_2 , since $1/T_{1,\parallel}T$ is much greater than $1/T_{1,\perp}T$, the relation can still be applicable.
- [44] D. Beeman and P. Pincus, Nuclear spin-lattice relaxation in magnetic insulators, *Phys. Rev.* **166**, 359 (1968).
- [45] C. Krellner, N. Caroca-Canales, A. Jesche, H. Rosner, A. Ormeci, and C. Geibel, Magnetic and structural transitions in layered iron arsenide systems: AFe_2As_2 versus RFeAsO , *Phys. Rev. B* **78**, 100504(R) (2008).
- [46] J. Zhao, W. Ratcliff II, J. W. Lynn, G. F. Chen, J. L. Luo, N. L. Wang, J. Hu, and P. Dai, Spin and lattice structures of single-crystalline SrFe_2As_2 , *Phys. Rev. B* **78**, 140504(R) (2008).
- [47] A. Jesche, N. Caroca-Canales, H. Rosner, H. Borrmann, A. Ormeci, D. Kasinathan, H. H. Klauss, H. Luetdens, R. Khasanov, A. Amato, A. Hoser, K. Kaneko, C. Krellner, and C. Geibel, Strong coupling between magnetic and structural order parameters in SrFe_2As_2 , *Phys. Rev. B* **78**, 180504(R) (2008).
- [48] D. W. Tam, W. Wang, L. Zhang, Y. Song, R. Zhang, S. V. Carr, H. C. Walker, T. G. Perring, D. T. Adroja, and P. Dai, Weaker nematic phase connected to the first order antiferromagnetic phase transition in SrFe_2As_2 compared to BaFe_2As_2 , *Phys. Rev. B* **99**, 134519 (2019).
- [49] J. M. Hastings and L. M. Corliss, First-order antiferromagnetic phase transition in MnS_2 , *Phys. Rev. B* **14**, 1995 (1976).
- [50] T. Chattopadhyay, H. G. v. Schnering, and H. A. Graf, First Order Antiferromagnetic Phase Transition in MnS_2 , *Solid State Commun.* **50**, 865 (1984).
- [51] B. C. Frazer, G. Shirane, D. E. Cox, and C. E. Olsen, Neutron-Diffraction Study of Antiferromagnetism in UO_2 , *Phys. Rev.* **140**, A1448 (1965).
- [52] C. G. Shull, W. A. Strauser, and E. O. Wollan, Neutron Diffraction by Paramagnetic and Antiferromagnetic Substances, *Phys. Rev.* **83**, 333 (1951).
- [53] D. Bloch, R. Maury, and C. Vetter, Order-Parameter and the Discontinuous Antiferro-Paramagnetic Transition in Manganese Oxide, *Phys. Lett.* **49A**, 354 (1974).
- [54] E. Fawcett, Spin-density-wave antiferromagnetism in chromium, *Rev. Mod. Phys.* **60**, 209 (1988).
- [55] N. G. Nereson, C. E. Olsen, and G. P. Arnold, Magnetic Structure of Europium, *Phys. Rev.* **135**, A176 (1964).
- [56] B. C. Gerstein, F. J. Jelinek, J. R. Mullaly, W. D. Shickell, and F. H. Spedding, Heat Capacity of Europium from 5° – 300°K , *J. Chem. Phys.* **47**, 5194 (1967).
- [57] R. L. Cohen, S. Hüfner, and K. W. West, First-Order Phase Transition in Europium Metal, *Phys. Rev.* **184**, 263 (1969).
- [58] P. Bak, S. Krinsky, and D. Mukamel, First-Order Transitions, Symmetry, and the ϵ Expansion, *Phys. Rev. Lett.* **36**, 52 (1976).
- [59] D. Mukamel and S. Krinsky, Physical realizations of the $n \geq 4$ -component vector models. I. Derivation of the Landau-Ginzburg-Wilson Hamiltonians, *Phys. Rev. B* **13**, 5065 (1976).
- [60] D. Mukamel and S. Krinsky, Physical realizations of the $n \geq 4$ -component vector models. II. ϵ -expansion analysis of the critical behavior, *Phys. Rev. B* **13**, 5078 (1976).
- [61] P. Bak and D. Mukamel, Physical realizations of the $n \geq 4$ -component vector models. III. Phase transitions in Cr, Eu, MnS_2 , Ho, Dy, and Tb, *Phys. Rev. B* **13**, 5086 (1976).
- [62] L. Zu, S. Lin, Y. Liu, J. C. Lin, B. Yuan, X. C. Kan, P. Tong, W. H. Song, and Y. P. Sun, A first-order antiferromagnetic-paramagnetic transition induced by structural transition in GeNCr_3 , *Appl. Phys. Lett.* **108**, 031906 (2016).